Supplementary Material

Erik M. YOUNG[1], Gwenn E. FLOWERS[1], Etienne BERTHIER[2], Rebecca LATTO[1*]

[1]*Department of Earth Sciences, Simon Fraser University, 8888 University Drive, Burnaby, British Columbia, V5A 1S6, Canada*

[2]*CNRS, Université de Toulouse, LEGOS, 14 avenue Ed. Belin, Toulouse 31400, France*

ABSTRACT.

*Present address: Mathematics and Physics, University of Tasmania, Private Bag 37, Hobart Tasmania 7001, Australia

MASS-BALANCE MODEL INPUTS

Potential direct clear-sky radiation

The potential direct clear-sky solar radiation is calculated using the solar analyst tool in the ArcGIS spatial analyst extension. The solar analyst tool calculates global, direct and diffuse solar radiation at discrete time intervals between sunrise and sunset at every gridcell in the modelled catchment. Direct solar radiation $I_{\theta,\alpha,t}$ is calculated using the relationship between sun position (given in azimuth α and zenith θ for discrete subdivisions of the sky area in regular sectors), atmospheric transmissivity (Fu and Rich, 1999; Tovar-Pescador and others, 2006) and the modelled location of the sun at every timestep as:

$$I_{\theta,\alpha,t} = I_0 \, \tau^{m(\theta)} \, SD_{\theta,\alpha,t} \, SG_{\theta,\alpha,t} \, \cos(\phi), \tag{1}$$

where I_0 is the solar constant of 1367 $\mathrm{W\,m^{-2}}$, τ is the atmospheric transmissivity set at a value of 0.75 typically used for clear sky conditions (Hock, 1998, 1999), $m(\theta)$ is the optical path length measured as a proportion of the zenith path, $SD_{\theta,\alpha,t}$ and $SG_{\theta,\alpha,t}$ are, respectively, the duration and fraction of insolation for discrete sky sectors, and ϕ is the angle between sky sector where the sun is located and the ground. The calculation is done at half-hourly intervals for every day of the year for both a standard calendar year and a leap year. The modelled solar geometry does not incorporate changes in atmospheric transmissivity, making the calculated radiation values insufficient for modelling mass balance several decades into the past or future (Wild and others, 2005; Huss and others, 2009), but adequate for modelling mass balance over multiple successive years. Given that the solar analyst tool does not account for daily changes in sunrise and sunset, an additional tool was developed that uses the PyEphem python astronomical calculations library to track local solar noon at the study location, and therefore provide local timestamps for the ArcGIS-derived direct solar radiation. The median time of insolation in modelled solar radiation values are assigned to the computed solar noon times in order to correctly assign timestamps to the modelled values.

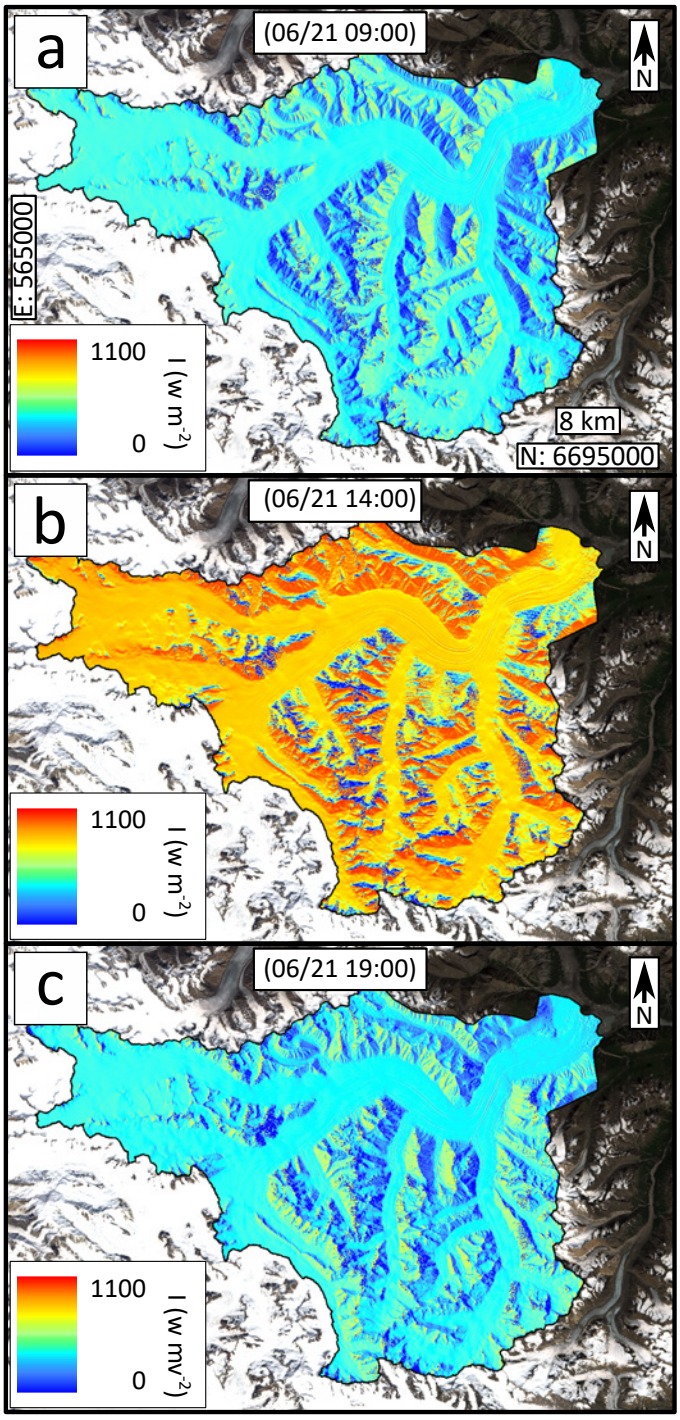

Fig. 1. Potential direct clear-sky solar radiation I used in melt model. Examples are shown for different times of day on 21 June. (a) 9:00, illumination from east. (b) 14:00, illumination from south. (c) 19:00, illumination from west. UTM (Zone 7 North) coordinates of southwest corner: 565000 E, 6695000 N.

Precipitation downscaling regression

At each time interval a series of coefficients $\beta = (b_0, b_1, b_2, b_3, b_4, b_5, b_6)$ is determined, where each coefficient relates precipitation to a local geographic predictor variable. In regions with mountainous topography, precipitation intensity can vary strongly with elevation and aspect, and to a lesser extent, with geographic proximity to coastal or inland areas of flat topography (Daly and others, 2008). Statistical downscaling methods often assume a linear aspect-dependent gradient in precipitation.

Only NARR data from the continental side of the St. Elias Mountains are incorporated in the precipitation regression for this study. We determine an optimal number of NARR grid points to use in the regression by incrementally adding grid points within an increasing radial distance from the centre of the catchment, and selecting the radius that produced the highest regression coefficients (four-gridcell radius, $\sim$ 128km). The downscaling method is adapted from Guan and others (2009). Daily timesteps are used to avoid the influence of local diurnal effects on precipitation that significantly weaken the performance of the downscaling method (Guan and others, 2009). Aspect is omitted due to the model being adapted for use in a single catchment trending roughly east–west, limiting regional-scale variation in drainage azimuth along the main orographic axis.

The regression is performed for each predictor and precipitation values at each NARR grid point (where $N_{\text{gridpoint}} \geq N_{\text{predictors}}$):

$$P = \frac{1}{n}\sum_{i=1}^{n}(b_0 + b_1X_i + b_2Y_i + b_3X_iY_i + b_4X_i^2 + b_5Y_i^2 + b_6Z_i)\ , \tag{2}$$

where X_i, Y_i and Z_i denote the Easting, Northing and elevation coordinates of the ith reanalysis grid point, and P is the NARR surface precipitation. The regression coefficients are then applied to the Easting, Northing and elevation coordinates of each local gridcell to determine the local precipitation p_{local}. For each model gridcell, downscaled precipitation ($p_{\text{downscaled}}$) is calculated as a combination of the raw NARR precipitation from the nearest grid point (p_{regional}) and p_{local}, based on the performance of the regression function at each timestep (Guan and others, 2009):

$$p_{\text{downscaled}} = p_{\text{local}}\, r_\beta^2 + p_{\text{regional}}(1 - r_\beta^2), \tag{3}$$

where r_β^2 is the correlation coefficient between NARR precipitation and the geographic predictors at every timestep.

Accumulation bias correction

Elevation (m a.s.l.)	ΔC
500	**1.26**
900	1.26
1100	1.23
1300	1.25
1500	1.28
1700	1.26
2100	1.24
2300	1.30
2500	2.47
2700	4.25
3100	5.45
3700	**5.45**

Table 1. Elevation-dependent accumulation bias-correction factors ΔC. Bold values are extrapolated.

Temperature bias correction

Month	Day of year	ΔT (°C)
Jan	15	−4.86
Feb	46	−3.98
Mar	74	−2.10
Apr	105	0.03
May	135	0.89
Jun	166	1.42
Jul	196	0.94
Aug	227	0.32
Sep	258	−0.32
Oct	288	−1.72
Nov	319	−4.37
Dec	349	−5.22

Table 2. Monthly temperature bias corrections ΔT. Values shown correspond to bias corrections applied at the middle of each month (Day of year) and are linearly interpolated between day numbers shown. Negative values indicate that NARR data overestimate AWS temperatures and vice versa.

Errors in downscaled temperature

Station ID	GL1		GL2		CC		DR		KDV		KCF		HJ		BL		Yearly means	
Year	RMSE	MAE	RMSE	MAE	RMSE	MAE	RMSE	MAE	RMSE	MAE	RMSE	MAE	RMSE	MAE	RMSE	MAE	RMSE	MAE
2007	1.92	1.45	1.97	1.46	2.19	1.69	2.02	1.66			2.01	1.78	4.66	3.36			2.46	1.90
2008	1.81	1.38	1.90	1.42	2.09	1.59	1.89	1.53			1.71	1.43	4.85	3.54			2.38	1.82
2009	1.78	1.35	1.83	1.37	2.08	1.59	1.85	1.45	1.92	1.82	1.64	1.31	4.69	3.35			2.26	1.75
2010	1.77	1.35	1.88	1.42	2.09	1.63	1.82	1.42	1.71	1.60	1.53	1.17	4.36	3.04			2.17	1.66
2011	1.79	1.35	1.86	1.40	2.15	1.68	1.85	1.42	1.66	1.50	1.62	1.24	4.27	3.01			2.17	1.66
2012	1.76	1.32	2.03	1.49	2.14	1.67	1.83	1.41	1.70	1.54	1.54	1.17	4.25	2.96	4.24	3.40	2.44	1.87
2013	1.75	1.31	2.11	1.54	2.15	1.68	1.85	1.42	2.14	1.71	1.54	1.17	4.33	3.00	4.42	3.52	2.54	1.92
2014	1.70	1.24			2.14	1.67	1.84	1.41	2.08	1.69	1.57	1.18	4.27	2.95	4.62	3.59	2.60	1.96
2015									2.00	1.62	1.59	1.18	4.29	2.97	4.68	3.50	3.14	2.32
2016									1.98	1.63	1.59	1.18	4.28	2.95	4.58	3.42	3.11	2.30
2017									1.95	1.63	1.61	1.21			4.59	3.40	2.72	2.08
Station means	1.79	1.34	1.94	1.44	2.13	1.65	1.87	1.47	1.90	1.64	1.63	1.28	4.42	3.14	4.52	3.47		
Station STD	0.06	0.06	0.10	0.06	0.04	0.04	0.06	0.09	0.17	0.10	0.14	0.18	0.22	0.23	0.16	0.08	0.33	0.49

Table 3. Error in downscaled monthly mean temperature (in °C prior to bias correction) evaluated with data from eight AWS locations: Glacier 1 (GL1), Glacier 2 (GL2), Canada Creek (CC), Duke River (DR), Kaskawulsh Divide (DV), Kaskawulsh Confluence (CF), Haines Junction (HJ), Burwash Landing (BL). RMSE and MAE are shown for each year in the respective AWS records. Station mean and standard deviation (STD) of the errors are shown at bottom. Annual mean RMSE and MAE are shown at right.

Station ID	GL1		GL2		CC		DR		KDV		KCF		HJ		BL		Monthly Means	
Month	RMSE	MAE	RMSE	MAE	RMSE	MAE	RMSE	MAE	RMSE	MAE	RMSE	MAE	RMSE	MAE	RMSE	MAE	RMSE	MAE
Jan	2.58	2.13	3.33	2.83	3.01	2.53	2.69	2.25	2.21	1.84	2.72	2.20	8.83	7.27	8.87	7.33	4.28	3.55
Feb	2.37	1.91	3.27	2.64	2.47	1.97	1.99	1.56	2.02	1.65	2.51	1.90	5.30	4.35	6.09	4.99	3.25	2.62
Mar	2.57	2.10	2.57	2.04	2.48	1.85	1.82	1.44	2.10	1.71	1.57	1.21	2.72	2.09	2.70	2.09	2.32	1.82
Apr	2.49	2.00	2.53	1.98	2.27	1.79	1.88	1.52	2.28	1.80	1.42	1.14	2.71	2.17	2.70	2.15	2.28	1.82
May	1.92	1.50	1.93	1.59	1.67	1.37	1.68	1.40	2.44	2.02	1.32	1.06	2.80	2.27	2.79	2.26	2.07	1.68
Jun	1.56	1.23	1.71	1.41	1.74	1.38	1.65	1.34	2.88	2.44	1.24	0.99	2.62	2.14	2.40	1.95	1.98	1.61
Jul	1.60	1.26	1.86	1.50	1.83	1.44	1.53	1.19	2.77	2.31	1.25	1.01	2.63	2.08	2.66	2.09	2.02	1.61
Aug	1.97	1.58	2.37	1.97	2.17	1.78	1.77	1.39	2.67	2.16	1.66	1.40	2.61	2.03	2.30	1.83	2.19	1.77
Sep	3.88	3.49	5.09	4.44	4.26	3.82	3.90	3.47	2.80	2.33	3.59	3.15	7.11	5.64	5.86	4.65	4.56	3.87
Oct	3.69	3.30	4.10	3.48	4.51	4.10	4.11	3.69	2.47	2.02	3.86	3.38	11.35	9.35	11.23	9.41	5.66	4.84
Nov	3.39	2.95	3.93	3.38	4.00	3.49	3.65	3.17	3.47	3.12	3.83	3.23	10.49	8.54	10.50	8.85	5.41	4.59
Dec	2.55	2.12	3.33	2.83	3.05	2.59	2.70	2.27	2.21	1.84	2.64	2.15	8.83	7.35	8.87	7.33	4.27	3.56
Station means	2.55	2.13	3.00	2.51	2.79	2.34	2.45	2.06	2.53	2.10	2.30	1.90	5.67	4.61	5.58	4.58	3.36	2.78
Station STD	0.76	0.75	1.02	0.93	0.99	0.97	0.94	0.90	0.41	0.40	1.02	0.91	3.45	2.86	3.46	2.93	1.40	1.23

Table 4. Error in downscaled three-hourly mean temperature (in °C prior to bias correction) evaluated with data from eight AWS locations: Glacier 1 (GL1), Glacier 2 (GL2), Canada Creek (CC), Duke River (DR), Kaskawulsh Divide (DV), Kaskawulsh Confluence (CF), Haines Junction (HJ), Burwash Landing (BL). RMSE and MAE are shown for each month in the respective AWS records. Station mean and standard deviation (STD) of the errors are shown at bottom. Monthly mean RMSE and MAE are shown at right.

MODEL TUNING

Snowline-elevation picks from satellite imagery

Date (YYYY-MM-DD)	Tributary	Snowline (m a.s.l.)
2019-08-04	SW	2477
2019-08-04	SA	2424
2018-08-23	SA	2216
2018-08-23	SW	2242
2018-08-01	NA	2208
2018-08-01	CA	1927
2017-08-06	NA	2278
2017-08-06	CA	2221
2017-08-08	SA	2196
2017-08-08	SW	2457
2016-09-08	SW	2474
2016-09-08	SA	2189
2014-09-08	NA	2233
2014-09-08	CA	2011
2013-09-05	SA	2220
2013-09-05	NA	2193
2013-09-05	CA	2308
2013-09-05	SW	2424
Mean ± std		2261 ± 150

Table 5. Snowline elevations picked from 2013–2019 satellite imagery of Kaskawulsh Glacier tributaries: North Arm (NA), Central Arm (CA), Stairway Glacier (SW), South Arm (SA).

Tuning results for debris-free case

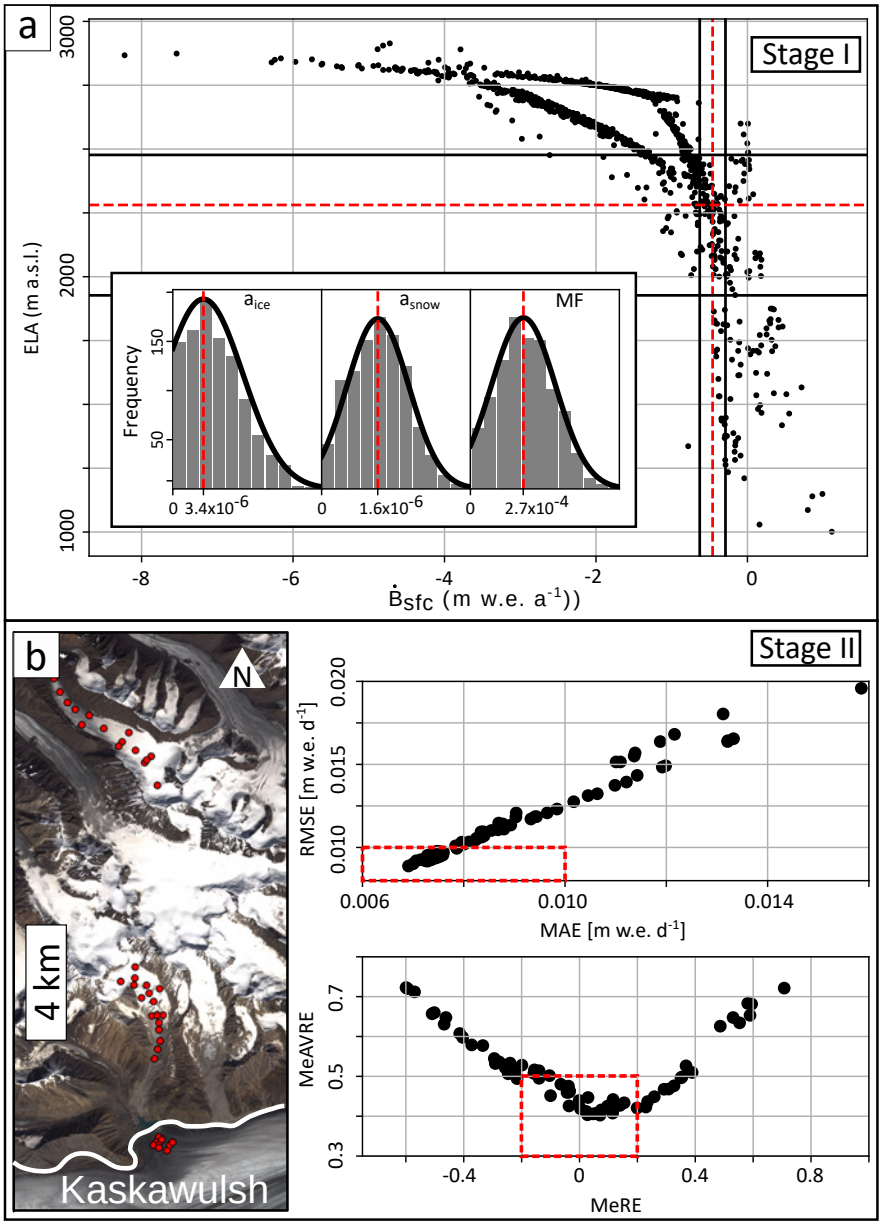

Fig. 2. Two-stage model tuning shown for debris-free simulations. The same procedure is carried out for debris-present simulations. (a) Stage 1. Modelled ELA versus glacier-wide mass balance for 2007–2018 for 1000 simulations (black dots) with values of *MF* (m w.e. $3h^{-1}\,°C^{-1}$), a_{ice} and a_{snow} (m w.e. $3h^{-1}\,°C^{-1}\,m^2\,W^{-1}$) randomly selected from normal distributions truncated at zero (inset). Observational targets (red dashed lines) are shown for ELA and glacier-wide mass balance. Simulations falling within the observational uncertainty (black lines) proceed to Stage 2. (b) Stage 2. RMSE versus MAE (top) and median of the absolute value of the relative error (MeAVRE) versus the median of the relative error (MeRE) between modelled and measured net ablation (bottom) at 44 locations (map at left). Simulations falling within both red dashed rectangles pass Stage 2.

MASS-BALANCE MODEL RESULTS

Standard deviation maps for mass-balance model results

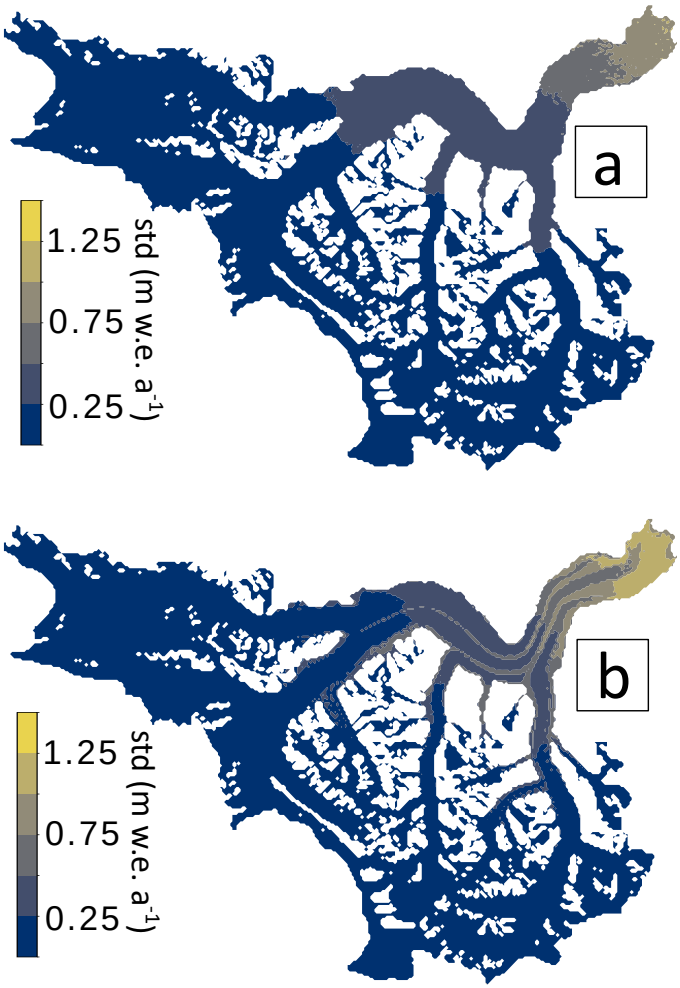

Fig. 3. Standard deviation (std) of modelled mass balance based on simulations that pass both stages of model tuning. (a) Debris-free case. (b) Debris-present case.

Balance fluxes for sensitivity tests

Transect ID	Reference		No ΔT		No ΔC		No RF		$T_{\mathrm{R2S}} = 0°\mathrm{C}$		$T_{\mathrm{R2S}} = 2°\mathrm{C}$	
	$Q_{\mathrm{bal}} \pm \sigma_Q$		$Q_{\mathrm{bal}} \pm \sigma_Q$		$Q_{\mathrm{bal}} \pm \sigma_Q$		$Q_{\mathrm{bal}} \pm \sigma_Q$		$Q_{\mathrm{bal}} \pm \sigma_Q$		$Q_{\mathrm{bal}} \pm \sigma_Q$	
NA	0.16	0.02	0.18	0.02	−0.09	0.02	0.07	0.01	0.15	0.02	0.17	0.02
CA	0.15	0.03	0.18	0.03	−0.16	0.03	−0.02	0.03	0.14	0.03	0.16	0.03
SW	0.13	0.01	0.14	0.01	−0.04	0.01	0.09	0.01	0.13	0.01	0.14	0.01
SA	0.11	0.02	0.13	0.02	−0.16	0.02	−0.01	0.02	0.10	0.02	0.12	0.02
KW5	0.23	0.06	0.26	0.05	−0.36	0.05	−0.08	0.04	0.20	0.06	0.25	0.06
KW4	0.15	0.07	0.17	0.05	−0.47	0.05	−0.19	0.05	0.12	0.07	0.18	0.07
KW3	0.19	0.08	0.20	0.06	−0.62	0.06	−0.23	0.07	0.15	0.08	0.22	0.08
KW2	0.06	0.08	0.05	0.06	−0.78	0.06	−0.40	0.08	0.02	0.08	0.09	0.08
KW1	−0.08	0.11	−0.07	0.08	−1.22	0.09	−0.69	0.11	−0.13	0.11	−0.03	0.11

Table 6. Balance fluxes Q_{bal} and standard deviations σ_Q at each flux gate for mass-balance model sensitivity tests applied to the debris-free case. Sensitivity tests are: disabling temperature bias correction (No ΔT), disabling accumulation bias correction (No ΔC), disabling refreezing parameterization (No RF) and changing rain-to-snow threshold temperature (T_{R2S}). Tributary flux gates are: North Arm (NA), Central Arm (CA), Stairway Glacier (SW), South Arm (SA). Flux gates along the main trunk are: KW5 (highest) to KW1 (lowest). All values in $\mathrm{km^3\,a^{-1}}$.

Transect ID	Reference		No ΔT		No ΔC		No RF		$T_{\mathrm{R2S}} = 0°\mathrm{C}$		$T_{\mathrm{R2S}} = 2°\mathrm{C}$	
	$Q_{\mathrm{bal}} \pm \sigma_Q$		$Q_{\mathrm{bal}} \pm \sigma_Q$		$Q_{\mathrm{bal}} \pm \sigma_Q$		$Q_{\mathrm{bal}} \pm \sigma_Q$		$Q_{\mathrm{bal}} \pm \sigma_Q$		$Q_{\mathrm{bal}} \pm \sigma_Q$	
NA	0.12	0.01	0.14	0.01	−0.11	0.01	0.04	0.01	0.11	0.01	0.13	0.01
CA	0.09	0.02	0.13	0.02	−0.21	0.02	−0.07	0.03	0.07	0.02	0.10	0.02
SW	0.12	0.01	0.13	0.01	−0.04	0.01	0.09	0.01	0.12	0.01	0.13	0.01
SA	0.08	0.02	0.11	0.02	−0.17	0.02	−0.02	0.02	0.07	0.02	0.09	0.02
KW5	0.11	0.03	0.17	0.03	−0.43	0.03	−0.15	0.05	0.08	0.03	0.14	0.03
KW4	0.02	0.04	0.07	0.04	−0.53	0.04	−0.27	0.06	−0.01	0.04	0.05	0.03
KW3	0.04	0.05	0.09	0.05	−0.68	0.05	−0.30	0.07	0.00	0.05	0.07	0.05
KW2	−0.09	0.06	−0.04	0.06	−0.82	0.06	−0.45	0.08	−0.13	0.06	−0.06	0.05
KW1	−0.21	0.09	−0.14	0.10	−1.20	0.09	−0.68	0.12	−0.27	0.09	−0.17	0.09

Table 7. Balance fluxes Q_{bal} and standard deviations σ_Q at each flux gate for mass-balance model sensitivity tests applied to the debris-present case. Sensitivity tests are: disabling temperature bias correction (No ΔT), disabling accumulation bias correction (No ΔC), disabling refreezing parameterization (No RF) and changing rain-to-snow threshold temperature (T_{R2S}). Tributary flux gates are: North Arm (NA), Central Arm (CA), Stairway Glacier (SW), South Arm (SA). Flux gates along the main trunk are: KW5 (highest) to KW1 (lowest). All values in $\mathrm{km}^3\,\mathrm{a}^{-1}$.

56 # ICE FLUXES

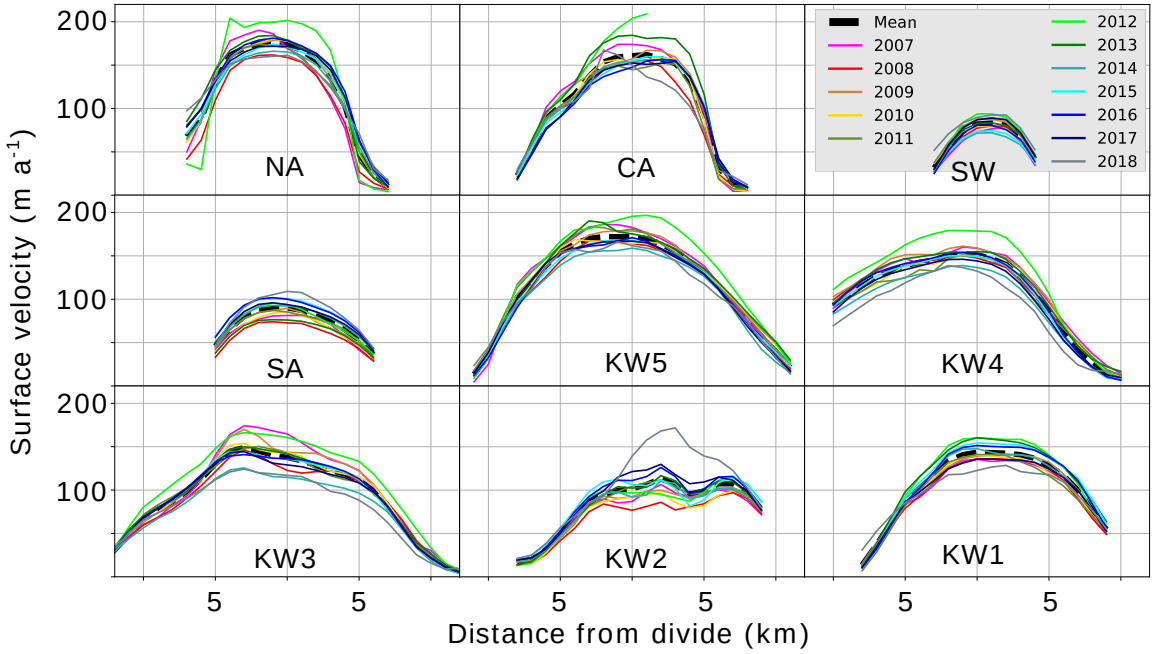

Fig. 4. Mean annual surface velocities for 2007–2018 at each flux gate. 2007–2018 mean is shown as bold dashed line. Tributary flux gates are: North Arm (NA), Central Arm (CA), Stairway Glacier (SW), South Arm (SA). Flux gates along the main trunk are: KW5 (highest) to KW1 (lowest). Velocity data generated using auto-RIFT (Gardner and others, 2018) and provided by the NASA MEaSUREs ITS_LIVE project (Gardner and others, 2019).

ANALYSIS AND INTERPRETATION

Continuity equation analysis for debris-free case

Flux Gate(s)	Surface Area	Gap fill	$\frac{\partial h}{\partial t}_{\text{obs}}$	$\frac{\partial h}{\partial t}_{\text{cal}}$	$\nabla \cdot q_{\text{obs}}$	$\nabla \cdot q_{\text{cal}}$	$\dot{B}_{\text{mod}}$	$\dot{B}_{\text{cal}}$
	km^2	%	m w.e. a^{-1}	m w.e. a^{-1}	m w.e. a^{-1}	m w.e. a^{-1}	m w.e. a^{-1}	m w.e. a^{-1}
NA	218	38	−0.18	−0.46	0.91	0.76	0.66	0.74
CA	319	17	−0.28	−0.38	0.59	0.61	0.43	0.31
SW	107	16	−0.32	0.78	0.35	1.52	1.13	0.03
SA	262	37	−0.40	0.13	0.26	0.78	0.39	−0.14
KW5	32	8	−0.80	0.24	−2.47	−2.05	−2.23	−3.28
KW4	22	15	−1.07	−2.65	−0.62	−3.01	−3.28	−1.69
KW3	22	45	−1.21	−2.17	−1.73	−3.31	−3.90	−2.93
KW2	29	49	−1.17	0.56	−4.64	−2.98	−4.08	−5.81
KW1	36	12	−1.53	−4.90	−1.37	−4.01	−6.27	−2.89
KW0	48	21	−1.55	−6.37	−3.27	−4.42	−9.64	−4.82
KW1+KW2	65	28	−1.37	−2.47	−2.85	−3.54	−5.28	−4.22
KW4+KW5	54	11	−0.91	−0.92	−1.73	−2.44	−2.65	−2.64
All tributaries	907	28	−0.29	−0.11	0.54	0.80	0.55	0.25
Main trunk	189	24	−1.17	−1.81	−2.25	−3.09	−4.06	−3.41
Glacier-wide	1096	28	−0.46	−0.49	0.00	0.07	−0.49	−0.46

Table 8. Independently estimated (subscript "obs" or "mod") versus calculated (subscript "cal") terms in the continuity equation for each section of the glacier (labelled with downstream flux gate): $\frac{\partial h}{\partial t}_{\text{cal}} = -\nabla \cdot q_{\text{obs}} + \dot{B}_{\text{mod}}$, $\dot{B}_{\text{cal}} = \frac{\partial h}{\partial t}_{\text{obs}} + \nabla \cdot q_{\text{obs}}$, $\nabla \cdot q_{\text{cal}} = \dot{B}_{\text{mod}} - \frac{\partial h}{\partial t}_{\text{obs}}$. Values of $\dot{B}_{\text{mod}}$ are for the debris-free case. Values of $\nabla \cdot q$ are converted to m w.e. a^{-1} using an ice density of $900\,\text{kg m}^{-3}$.

REFERENCES

Daly C and 7 others (2008) Physiographically sensitive mapping of climatological temperature and precipitation across the conterminous United States. *International Journal of Climatology: a Journal of the Royal Meteorological Society*, **28**(15), 2031–2064 (doi: 10.1002/joc.1688)

Fu P and Rich PM (1999) Design and implementation of the Solar Analyst: an ArcView extension for modeling solar radiation at landscape scales. In *Proceedings of the nineteenth annual ESRI user conference*, volume 1, 1–31, San Diego USA

Gardner AS and 6 others (2018) Increased West Antarctic and unchanged East Antarctic ice discharge over the last 7 years. *Cryosphere*, **12**(2), 521–547 (doi: 10.5194/tc-12-521-2018)

Gardner AS, Fahnestock MA and Scambos TA (2019) ITS_LIVE Regional Glacier and Ice Sheet Surface Velocities. (doi: 10.5067/6II6VW8LLWJ7), data archived at National Snow and Ice Data Center

Guan H, Wilson JL and Xie H (2009) A cluster-optimizing regression-based approach for precipitation spatial downscaling in mountainous terrain. *Journal of Hydrology*, **375**(3-4), 578–588 (doi: 10.1016/j.jhydrol.2009.07.007)

Hock R (1998) *Modelling of glacier melt and discharge*. Ph.D. thesis, ETH Zurich

Hock R (1999) A distributed temperature-index ice-and snowmelt model including potential direct solar radiation. *Journal of Glaciology*, **45**(149), 101–111 (doi: 10.3189/S0022143000003087)

Huss M, Funk M and Ohmura A (2009) Strong alpine glacier melt in the 1940s due to enhanced solar radiation. *Geophysical Research Letters*, **36**(23) (doi: 10.1029/2009GL040789)

Tovar-Pescador J, Pozo-Vázquez D, Ruiz-Arias J, Batlles J, López G and Bosch J (2006) On the use of the digital elevation model to estimate the solar radiation in areas of complex topography. *Meteorological Applications*, **13**(3), 279–287 (doi: 10.1017/S1350482706002258)

Wild M and 9 others (2005) From dimming to brightening: Decadal changes in solar radiation at Earth's surface. *Science*, **308**(5723), 847–850 (doi: 10.1126/science.1103215)